Applied Catalysis B: Environmental 236 (2018) 45–52

Contents lists available at ScienceDirect

# Applied Catalysis B: Environmental

journal homepage: www.elsevier.com/locate/apcatb

# Fabrication of graphitic-$C_3N_4$ quantum dots/graphene-$InVO_4$ aerogel hybrids with enhanced photocatalytic NO removal under visible-light irradiation

Jundie Hu, Dongyun Chen*, Najun Li, Qingfeng Xu, Hua Li, Jinghui He, Jianmei Lu*

*College of Chemistry, Chemical Engineering and Materials Science, Collaborative Innovation Center of Suzhou Nano Science and Technology, Soochow University, Suzhou, 215123, China*

ARTICLE INFO

*Keywords:*
Graphitic $C_3N_4$ quantum dots
3D aerogel
NO removal
Visible-light irradiation
Recyclable

ABSTRACT

A new 3D aerogel of CNQDs/GO-$InVO_4$ (CNQDs = graphitic $C_3N_4$ quantum dots, GO = graphene oxide) with porous layered structure is fabricated successfully. The stable and recyclable macro-material is found to be highly suitable for practical application. CNQDs with an average diameter of 3.0 nm are prepared through the exfoliation of bulk g-$C_3N_4$ step by step, and are decorated on the surface of GO uniformly by electrostatic, π—π stacking and hydrogen-bonding interactions. The CNQDs/GO are wrapped tightly around cubic $InVO_4$, resulting in the immediate formation of a 3D aerogel with a heterostructure. The synergistic heterojunction exhibit a powerful photocatalytic effect for the removal of NO at the ppb-level (600 ppb) under visible-light irradiation, with a maximum efficiency up to 65%. A Z-scheme photocatalytic mechanism is proposed based on ESR experiments and calculation of the energy bands.

## 1. Introduction

Atmospheric pollution is recognized as one of the most severe challenges facing modern societies [1–3]. Among the especially serious consequences are haze events [4–6], photochemical smog [7–8] and PM 2.5 [9–10] (the emission of particulate matter with diameter less than 2.5 μm), all of which are caused by the formation of secondary aerosols. Nitrogen oxides ($NO_x$, consisting of NO and $NO_2$) are important secondary aerosol precursors, and their removal is an important goal in environmental protection [11]. Graphitic carbon nitride (g-$C_3N_4$), with a band gap of about 2.7 eV, is an effective metal-free semiconductor that has been used as a photocatalyst because of its two-dimensional (2D) structure, visible-light response, extraordinary stability and low cost of production [12–18]. Despite these remarkable properties, pristine g-$C_3N_4$ performs unsatisfactorily because of limitations such as extremely rapid recombination of the electron-hole ($e^-$-$h^+$) pairs, poor electrical conductivity, small surface area and inefficient absorption of visible light [19]. Therefore, numerous efforts to overcome these drawbacks have been made, such as chemical modification [20–22], element doping [23–25] and the construction of heterojunctions [26–33]. Alternatively, a novel and effective approach is conversion of the 2D material into a 0D material through the creation of g-$C_3N_4$ quantum dots (CNQDs). This system is a promising photocatalyst, attributed to its high electrical conductivity, photostability and abundance of exposed catalytically active sites, such as edge $NH/NH_2$ groups, pyridinic N and graphitic N [34–37]. Promisingly, g-$C_3N_4$ can be easily combined with the highly conductive graphene oxide (GO) through electrostatic, π-π stacking and hydrogen-bonding interactions [38–39].

Despite the numerous attractive characteristics of CNQDs, they are still unsuitable as photocatalysts when prepared in pure form. As noted above, the photocatalytic effectiveness of g-$C_3N_4$ can be improved through the construction of g-$C_3N_4$-based heterojunctions, such as g-$C_3N_4/Bi_2O_2CO_3$ [40], g-$C_3N_4/Bi_2WO_6$ [41], g-$C_3N_4/TiO_2$ [28], and g-$C_3N_4/MoS_2$ [42]. In this context, indium vanadate ($InVO_4$), with a band gap of about 2.3 eV, is an important visible-light-responsive photocatalyst as a result of its adequate utilization of visible light, controllable morphology and size, and simple hydrothermal synthesis [43–44]. $InVO_4$ has received extensive attention in various application fields, such as degradation of organic pollutants, treatment of exhaust gases, and water splitting. Therefore, the construction of a heterojunction between CNQDs and $InVO_4$ nanoparticles is an extremely attractive possibility for the photocatalytic degradation of NO under visible-light irradiation.

However, catalysts in conventional powder form suffer from several drawbacks in industrial applications: for instance, they are easily blown

* Corresponding authors.
*E-mail addresses:* dychen@suda.edu.cn (D. Chen), lujm@suda.edu.cn (J. Lu).

https://doi.org/10.1016/j.apcatb.2018.04.080
Received 8 March 2018; Received in revised form 21 April 2018; Accepted 30 April 2018
Available online 01 May 2018
0926-3373/ 

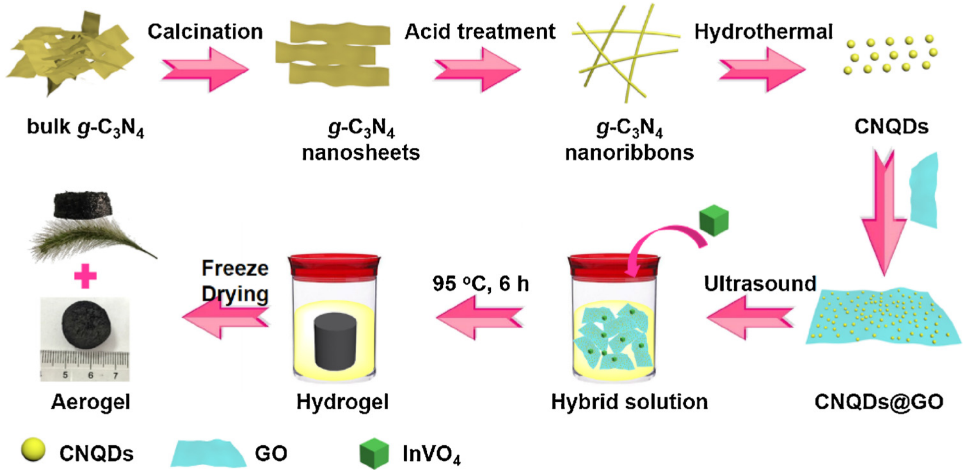


**Scheme 1.** Schematic diagram of the synthesis of CNQDs/GO-$InVO_4$ aerogel.

away in the air, difficult to recycle, and environmentally hazardous. A possible solution is the construction of macro-materials, *i.e.* the immobilization of powder catalysts on a macro-structure, for example on the surface of carbon cloth, foam, sponge or aerogel [45–49].

Herein, a 3D CNQDs/GO-$InVO_4$ aerogel is fabricated successfully for the first time *via* the exfoliation and template-free hydrothermal methods. A schematic of its synthesis process is displayed in Scheme 1. Bulk g-$C_3N_4$ is decomposed into CNQDs step by step, and then the CNQDs, with diameters of about 3 nm, are dispersed on the surface of GO uniformly. Then, the CNQDs/GO are wrapped tightly around freshly synthesized cubic $InVO_4$, resulting in the immediate formation of a 3D structure and heterojunction. The 3D structure can be likened to pearls decorated on a gauze. The CNQDs/GO-$InVO_4$ aerogel is evaluated for photocatalytic activity in the removal of NO at the ppb-level under visible-light irradiation. Its high performance is mainly attributed to synergistic effects and intimate interfacial contact in CNQDs/GO-$InVO_4$. A Z-scheme photocatalytic mechanism is also proposed based on ESR spin-trapping experiments and calculation of the energy bands.

## 2. Experimental

### 2.1. Materials

Dicyandiamide and graphite powder (purity > 99.7%) were purchased from Sigma Aldrich. Concentrated sulfuric acid ($H_2SO_4$), phosphoric acid ($H_3PO_4$), nitric acid ($HNO_3$), hydrogen peroxide ($H_2O_2$, 30%), ammonium hydroxide ($NH_3{\cdot}H_2O$), thylenediamine (EDA) and microporous membrane (0.45 μm, 0.22 μm) were purchased from Sinopharm Chemical ReagentCo., Ltd (China). $In(NO_3)_3{\cdot}4.5H_2O$, $NH_4VO_3$ and polyvinylpyrrolidone (PVP) were purchased from Tokyo Chemical Industry. 5,5-dimethyl-l-pyrroline-*N*-oxide (DMPO) was purchased from Biorbyt. All the chemicals were analytical reagent and used without further purification.

### 2.2. Characterization

The morphologies and elemental analysis of the samples were performed by the scanning electron microscopy (SEM) (Hitachi S-4800). Transmission electron microscopy (TEM), high-resolution transmission electron microscopy (HRTEM) images, element mapping and selected area electron diffraction (SAED) of the products were observed on the Hitachi H600 with 200 kV acceleration voltage. The crystallographic structure were characterized by X-ray diffraction (XRD) and carried out on a X'Pert-Pro MPD. X-ray photoelectron spectrometer (ESCALAB MK II, Al-Kα radiation as the exciting source) was used to obtain the X-ray photoelectron spectroscopy (XPS) spectra, the valence band (VB) edges of the photocatalysts were also estimated by XPS. The optical properties of the samples were investigated by Fourier transform-IR spectroscopy (FT-IR) (Nicolet 4700), Raman spectra (Renishaw Invia, UK, excitation wavelength = 532 nm), Photoluminescence (PL) spectra (FLS920, excitation wavelength = 360 nm) and UV–vis spectrophotometer (CARY50, $BaSO_4$ as the reflectance sample). Photocurrent and electrochemical impedance spectroscopy (EIS) were implemented on CHI 660B electrochemical system (Shanghai, China) to study the electrochemical properties of the as-prepared samples. JES-X320 spectrometer was used to record Electron spin resonance (ESR) spectra which detect the signals of $\cdot OH$ and $\cdot O_2^-$, 50 mM DMPO solution was used as paramagnetic species spin-trap agent (methanol dispersion for $\cdot O_2^-$ trapping and aqueous dispersion for $\cdot OH$ trapping). Thermo Environmental Instruments, Inc, 42i-TL was used to recorded the process of photocatalytic degradation of NO.

### 2.3. Preparation of $C_3N_4$ QDs and $InVO_4$

$C_3N_4$ QDs and $InVO_4$ were synthesized by the exfoliation method and hydrothermal method, respectively, and detailed process were displayed in the Supporting Information (S1, S2).

### 2.4. Preparation of CNQDs/GO-$InVO_4$ aerogels

GO was prepared according to Hummer's method by oxidation of graphite powder [50]. The aerogel was synthesized *via* a hydrothermal method as the following steps: 10 mL CNQDs solution was placed into a glass vial (20 mL), 15 mg GO was added to the above solution and stirred for 2 h to form an evenly system, then various molar ratios of $InVO_4$ was added and stirred for another 1 h and 30 μL of EDA was introduced. The mixture was heated at 95 °C for 6 h to obtain a columnar hydrogel, the CNQDs/GO-$InVO_4$ aerogel was formed after freeze drying for 48 h. The aerogels were denoted as CNQDs/GO-$InVO_4$ 10, CNQDs/GO-$InVO_4$ 20, CNQDs/GO-$InVO_4$ 30, CNQDs/GO-$InVO_4$ 40 and CNQDs/GO-$InVO_4$ 50, where the molar ratio of $InVO_4$ was 10%, 20%, 30%, 40% and 50%, respectively. A series of CNQDs/GO (mass ratio of CNQDs is 25%, 50%, 75% and 90%) aerogels were also synthesized according to the above method without $InVO_4$ nanoparticles, which are denoted as CNQDs/GO-25, CNQDs/GO-50, CNQDs/GO-75, CNQDs/GO-90, respectively.

### 2.5. Photoelectrochemical experiments

Photoelectrochemical experiments (photocurrent responses and electrochemical impendance spectra (EIS)) were performed on a CHI 660B electrochemical station with a conventional three-electrode

system and $Na_2SO_4$ aqueous solution (0.1 M) as electrolyte. While Pt wire and Ag/AgCl were chosen as the counter electrode, and reference electrode, respectively. 8 mg photocatalysts were loaded on the surface of indium-tin oxide (ITO) glass (1 cm × 4 cm) evenly, which was chosen as the working electrode. In this experiment, a 300 W Xenon lamp was used as the light source.

### 2.6. Photocatalytic activity measurements

The photocatalytic activity of the synthesized samples were evaluated by the efficiency of NO (600 ppb level) removal in a cylindrical continuous flow reactor with a volume of 2.26 L ($\pi R^2 H = \pi \times m^2 \times 20$ cm) at ambient temperature under visible light irradiation. The photocatalysts (50 mg) were coated on the middle of square board (4 cm × 4 cm), which was placed in the center of glass reactor. The NO (600 ppb) was acquired by adjusting the proportion of NO gas (10 ppm, $N_2$ balance) and air stream, and the flow rate of the mixture gas stream was controled at 1.2 L $min^{-1}$. A 300 W commercial Xenon lamp which was vertically placed on the reactor was switched on after adsorption-desorption equilibrium (keep in dark for 30 min). The concentration of NO was monitored every minute by the $NO_x$ (NO and $NO_2$) analyzer (Thermo Environmental Instruments, Inc., 42i-TL). The NO removal ratio (η) was calculated as $\eta\ (\%) = (1 - C/C_0) \times 100\%$, where $C$ and $C_0$ are concentrations of NO in the outlet and feeding stream, respectively. The consecutive cycle experiments were also accomplished by the above method.

## 3. Results and discussion

### 3.1. Phase and composition

The phase composition and crystal structure of GO, CNQDs, $InVO_4$ and a series of CNQDs/GO-$InVO_4$ aerogels were characterized by XRD (Fig. 1). A distinct diffraction peak appeared at 9.9° in GO, which was attributed to the (002) plane of GO. However, in the XRD of the CNQDs/GO-$InVO_4$ aerogels, the diffraction peak at 9.9° disappeared, because the oxygen-containing functional groups on the surface of GO were reduced by ethylenediamine [51]. However, a new peak appeared at about 25.1°, which was overlapped by the diffraction peak of CNQDs at 27.3°. The XRD pattern revealed that the phase composition of CNQDs was similar to bulk CN, indicating that the crystal structure was unchanged after decomposition to CNQDs and the tri-*s*-triazine units were retained. Notably, the intensity of the peak of CNQDs/GO-$InVO_4$ aerogels at 27.3° ((002) plane of CNQDs) was gradually weakened with the increasing content of $InVO_4$. Promisingly, the diffraction peaks of pure $InVO_4$ nanoparticles matched well with the standard card (JCPDS No. 48-0898). All the peaks of $InVO_4$ could be identified in the XRD of CNQDs/GO-$InVO_4$ aerogels, demonstrating that the synthesis process of the aerogel did not damage the crystal structure of $InVO_4$.

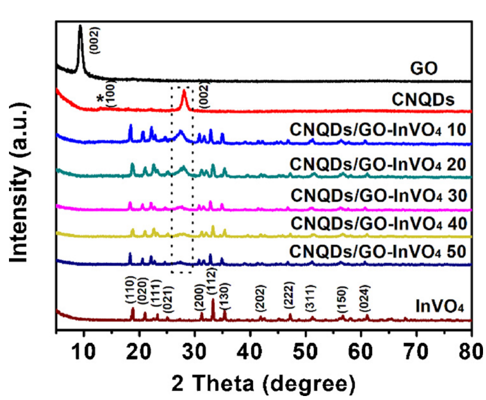


**Fig. 1.** XRD patterns of GO, CNQDs, pure $InVO_4$ and CNQDs/GO-$InVO_4$ aerogels.

XPS was performed to analyze the surface chemical states and elemental composition of the as-prepared CNQDs/GO-$InVO_4$ 30 aerogel (Fig. 2). The XPS survey spectrum in Fig. 2a shows that the aerogel was composed of C, N, O, In and V elements. Fig. 2b shows that the C 1s spectra could be divided into four peaks, corresponding to C−N−C (288.25 eV), N−C═N (287.64 eV), C−OH/C−O−C (286.79 eV) and C−C (284.90 eV) [47,51]. Three distinct peaks were observed in the N 1s curve (Fig. 2c), among which the binding energy of 400.10 eV can be assigned to the tertiary nitrogen N−$(C)_3$ groups, the peak at 399.12 eV corresponds to pyridinic N, and the binding energy of 398.48 eV is attributed to C═N−C [47,51]. Meanwhile, the O 1s spectrum showed three peaks at 532.64 eV, 531.50 eV and 530.97 eV, corresponding to the –OH from the surface of GO and CNQDs (partially acidified), C−O bonds, and the oxygen from $InVO_4$, respectively. Fig. 2e reveals that In 3d possesses two binding energies at 451.46 and 443.85 eV, assigned to In $3d_{3/2}$ and In $3d_{5/2}$, respectively [43,52]. Meanwhile, the signals of V $2p_{1/2}$ and V $2p_{3/2}$ were captured at 524.16 and 516.82 eV, respectively [43,52].

Fig. 3a displays the FT-IR spectra of GO, CNQDs, $InVO_4$ and CNQDs/GO-$InVO_4$ 30 aerogel. The absorption bands of GO at > 3000 and 1724 $cm^{-1}$ were attributed to the stretching vibration of O−H and C═O bonds, respectively. The characteristic peaks of CNQDs at about 3200, 1640–1240 and 806 $cm^{-1}$ were assigned to the stretching mode of N−H and O−H bonds, heterocycles and triazine units, respectively. The FT-IR spectrum of $InVO_4$ exhibited the vibration of V−O−In (900 $cm^{-1}$), V−O (950 $cm^{-1}$) and $VO_4^{3-}$ (750 $cm^{-1}$). However, the CNQDs/GO-$InVO_4$ 30 aerogel displayed all the above absorption peaks, confirming that the aerogel is a composite of all three species. Raman spectroscopy provided further evidence for the existence of GO and CNQDs in the aerogel. The two peaks at 1330 and 1600 $cm^{-1}$ correspond to the D and G bands of GO, respectively. The $I_D/I_G$ peak intensity ratios of GO and CNQDs/GO-$InVO_4$ 30 aerogel are 0.83 and 0.92, respectively, indicating the high crystallinity of GO in both samples. The increased $I_D/I_G$ ratio for CNQDs/GO-$InVO_4$ 30 aerogel is caused by the introduction of CNQDs (1560 $cm^{-1}$) and $InVO_4$, as displayed in Fig. 3b.

### 3.2. Morphology of the photocatalysts

The morphologies of the as-prepared samples were investigated by TEM, HRTEM, SAED, TEM mapping, SEM and SEM–energy dispersive spectroscopy (SEM-EDS). The 0D CNQDs were synthesized *via* the exfoliation of bulk g-$C_3N_4$, in which process g-$C_3N_4$ nanosheets and g-$C_3N_4$ nanoribbons (as shown in **Fig. S1**) were formed, before CNQDs were finally obtained. As illustrated in Fig. 4**a**, the TEM image of CNQDs demonstrated that these quantum dots were dispersed evenly and had diameters in the range of 1–5 nm, with an average diameter of 3.0 nm (calculated by the software Nano Measurer 1.2.5 on the basis of TEM). The small diameter size endows CNQDs with strong quantum confinement and edge effects, which ensures that CNQDs could intimately anchor on the surface of grapheme by π−π stacking interactions. The HRTEM image of CNQDs (Fig. 4d) revealed a lattice spacing of about 0.336 nm, which is consistent with the (002) plane of g-$C_3N_4$, indicating that the CNQDs possessed very high crystallinity. The TEM images of CNQDs/GO-$InVO_4$ 30 aerogel (Fig. 4b–c) showed the transparent structure of GO, upon which CNQDs were uniformly decorated through the electrostatic, π−π stacking and hydrogen-bonding interactions between CN and GO. Meanwhile, $InVO_4$ cubes were tightly wrapped by the CNQDs-modified GO. A lattice spacing of 0.274 nm can be seen in the HRTEM image of $InVO_4$ (Fig. 4e), corresponding to the (112) plane of $InVO_4$. The SAED pattern of $InVO_4$ (Fig. 4f) showed a series of concentric diffraction rings, indicating the polycrystalline nature of $InVO_4$. The rings from inside to outside (marked by red arrows) were indexed to the (112), (130), (200), (311) and (024) crystal planes of $InVO_4$, which matched with the standard card (JCPDS No. 48-0898).

Fig. 5a shows the SEM image of pure $InVO_4$ cubes, indicating the

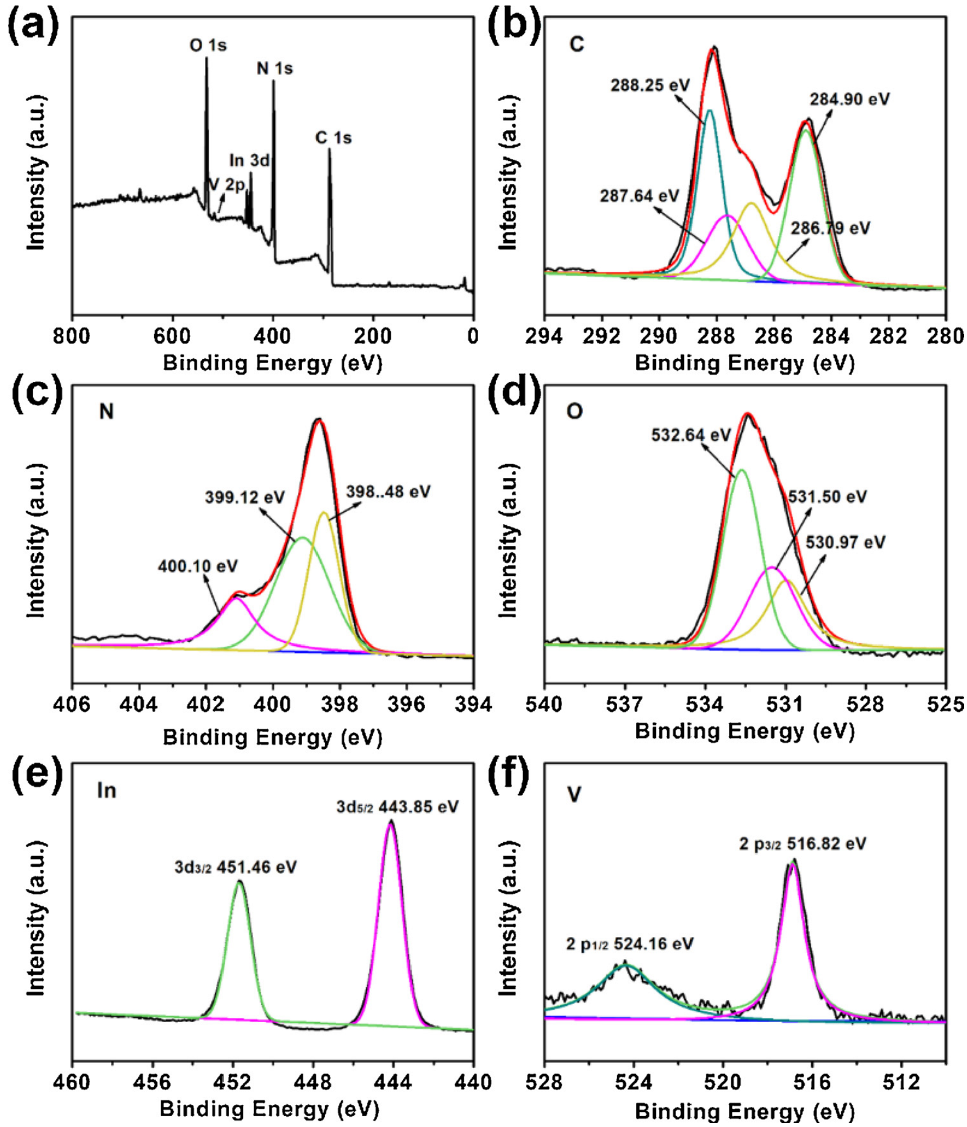


**Fig. 2.** XPS spectra of CNQDs/GO-$InVO_4$ 30 aerogel: (a) survey, (b) C 1s, (c) N 1s, (d) O 1s, (e) In 3d and (f) V 2p.

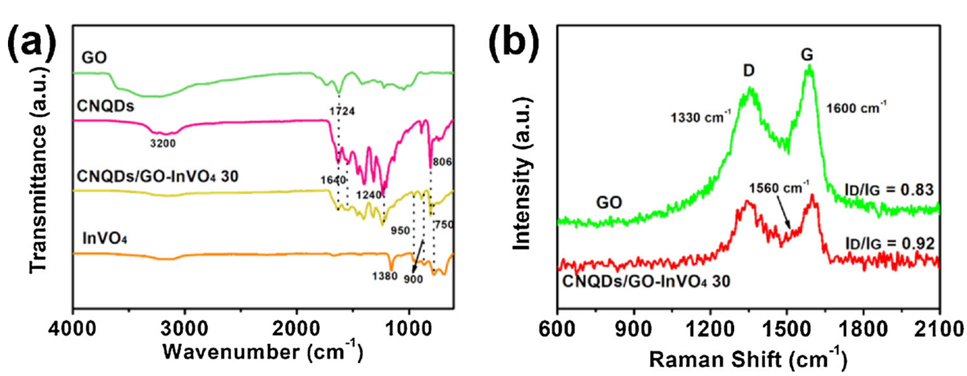


**Fig. 3.** (a) FTIR spectra and (b) Raman spectra of the as-prepared samples.

size of the $InVO_4$ cubes as about 200–300 nm. As illustrated in Fig. 5b–c, the interconnected 3D CNQDs/GO-$InVO_4$ 30 aerogel exhibits a porous layered structure, in which the $InVO_4$ cubes were evenly wrapped by the wrinkled CNQDs/GO, resembling pearls inlaid on a gauze. The micro-structure of the CNQDs/GO-$InVO_4$ 30 aerogel heterojunction was also explored by EDS elemental mapping, indicating the existence of the elements C, N, O, In and V (Fig. 5d–i). Moreover, SEM-EDS analysis (Fig. S2, supporting information) of CNQDs/GO-$InVO_4$ 30 aerogel further verified the presence of those elements.

### 3.3. Optical properties

The optical properties of the as-synthesized photocatalysts were examined by UV–vis DRS and PL spectroscopy. Fig. 6a depicts the

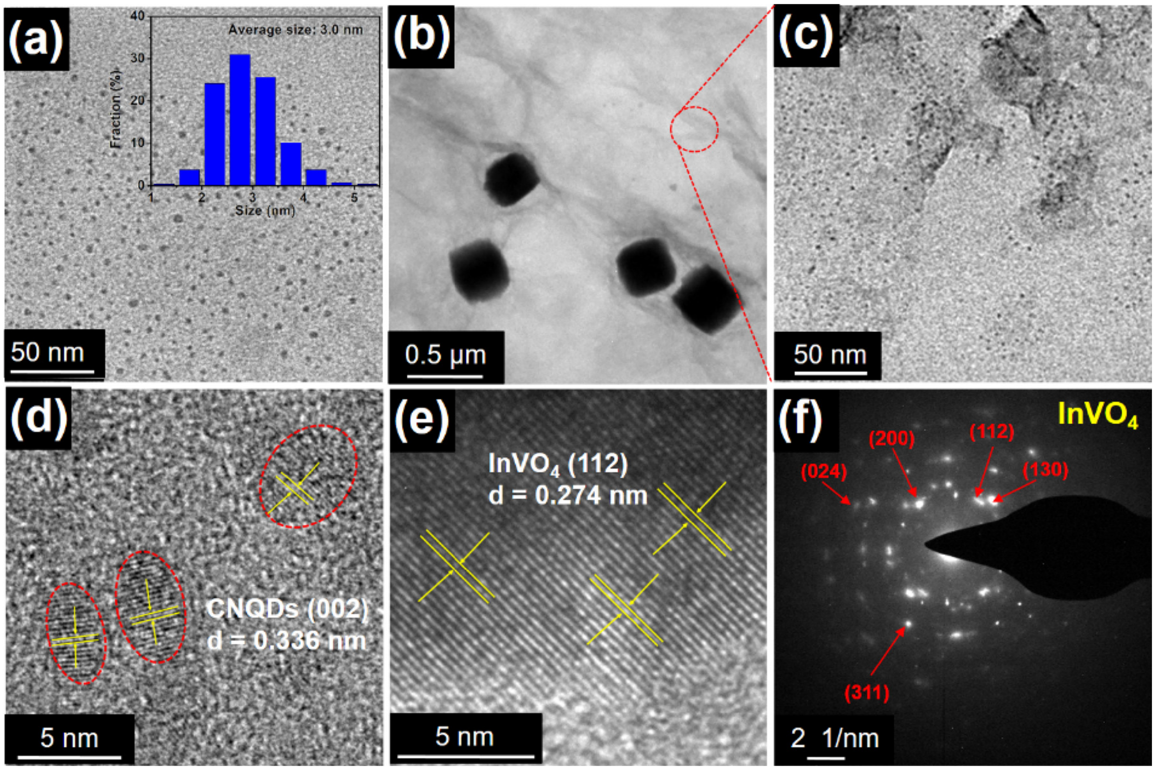


**Fig. 4.** (a) TEM image and the corresponding size distribution of the CNQDs, (b–c) TEM images of CNQDs/GO-$InVO_4$ 30 aerogel, HRTEM images of (d) CNQDs and (e) $InVO_4$, (f) SAED pattern of $InVO_4$.

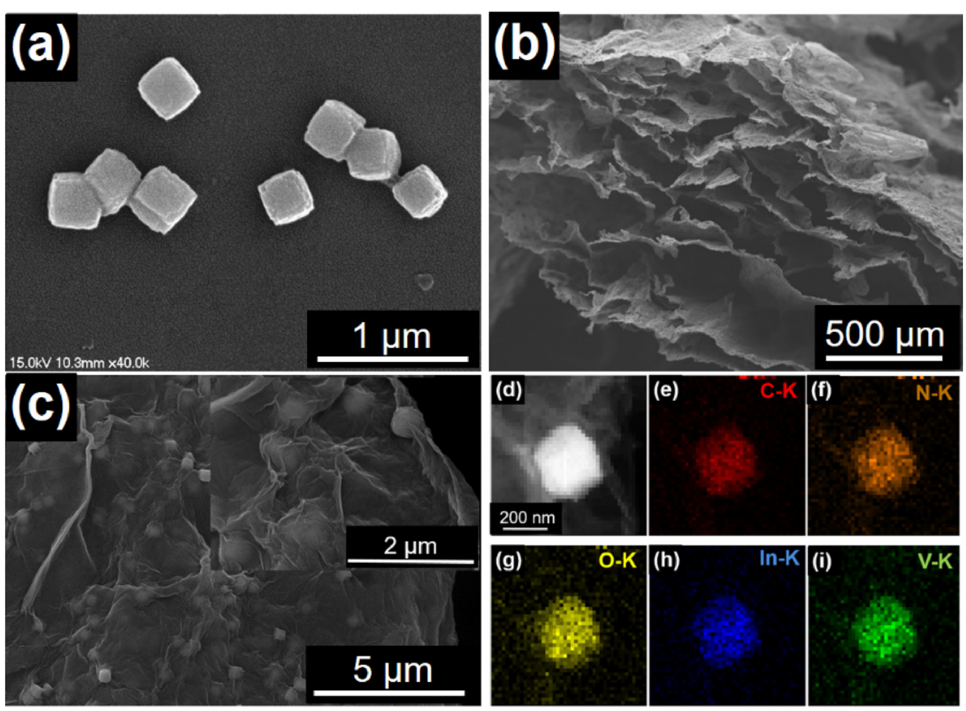


**Fig. 5.** SEM images of (a) $InVO_4$, (b–c) CNQDs/GO-$InVO_4$ 30 aerogel, (d) TEM image of CNQDs/GO-$InVO_4$ 30 aerogel and EDS mapping images of (e) C, (f) N, (g) O, (h) In and (i) V.

UV–vis DRS spectra of bulk CN, CNQDs, $InVO_4$ and CNQDs/GO-$InVO_4$ aerogels. It is clear that the absorption peak of the CNQDs was similar in position and intensity to that of bulk CN. CNQDs and $InVO_4$ displayed prominent absorption edges at about 430 nm and 680 nm, respectively, belonging to the visible-light region. As expected, the CNQDs/GO-$InVO_4$ aerogels exhibited absorption at both 430 nm and 680 nm, indicating that the wavelength range of visible-light absorption of the photocatalyst was widened by the introduction of $InVO_4$. In addition, the band gap energies of CNQDs and pure $InVO_4$ were calculated from the Tauc plots ($(\alpha h\nu)^2 = A(h\nu - E_g)$). The calculated band gaps were about 2.64 eV for CNQDs and 2.37 eV for $InVO_4$ (Fig. 6b). To calculate the valence band (VB) and conduction band (CB) levels of the

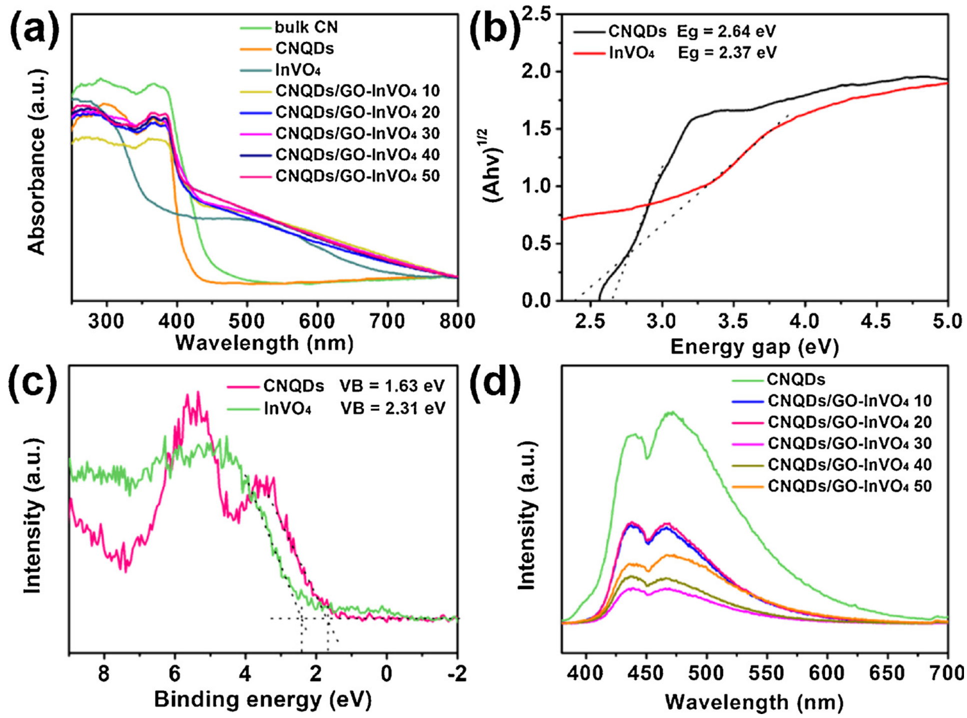


**Fig. 6.** (a) UV–vis DRS spectra of as-prepared samples, (b) estimated band gap and (c) VB XPS of CNQDs and $InVO_4$ and (d) photoluminescence (PL) spectra (excitation wavelength = 360 nm) of the products.

photocatalysts, the VB edges of CNQDs and $InVO_4$ were estimated to be 1.63 and 2.31 eV, respectively, by referring to the VB XPS spectra, as displayed in Fig. 6c. Thus, the CB edges of CNQDs and $InVO_4$ were calculated to be −1.01 and −0.06 eV (Fig. 10).

The PL spectra of CNQDs and CNQDs/GO-$InVO_4$ aerogels were detected under the excitation wavelength of 360 nm, as shown in Fig. 6f. Two emission peaks at about 435 nm and 475 nm can be attributed to the transition from $\delta^*$-LP (lone pair) and $\pi^*$-LP states [45]. The PL emission intensity was sharply reduced after the formation of aerogels. The CNQDs/GO-$InVO_4$ 30 aerogel exhibited the lowest signal, which indicated the most efficient charge separation of photo-induced $e^-$-$h^+$ pairs, conducive to the enhancement of photocatalytic activity.

### 3.4. Photoelectrochemical properties

To investigate the effect of the heterojunction on the enhancement of photocatalytic activity, electrochemical experiments, including transient photocurrent response and EIS, were conducted. These experiments gave information on the transfer and separation of the photogenerated charge: a higher current density suggests a more effective separation and transfer of photogenerated $e^-$−$h^+$ pairs. Fig. 7a shows that the current density of CNQDs was greater than that of bulk CN, indicating that the CNQDs exhibit greater ability to separate the $e^-$-$h^+$ pairs and conduct the resulting electronic charge. The photocurrent response of the CNQDs/GO-$InVO_4$ aerogels was considerably greater than for the bare CNQDs. The highest photocurrent was achieved by the CNQDs/GO-$InVO_4$ 30 aerogel, which was 6 times higher than that of CNQDs. Thus, the construction of a heterojunction was beneficial to the photocatalytic effect. The same conclusion could be drawn from the EIS spectrum of CNQDs/GO-$InVO_4$ 30 aerogel, which featured the smallest arc radius among all samples, as displayed in Fig. 7b.

### 3.5. Photocatalytic performances for NO removal

The photocatalytic activities of the as-prepared photocatalysts were evaluated by the removal of NO (ppb-level) under visible-light irradiation to assess their potential capability in air purification (Fig. 8a). Adsorption/desorption equilibrium between the mixture gas and samples was achieved before the reactions were started. As a preliminary step, CNQDs/GO aerogels with different mass ratios were applied in the NO removal experiments, and CNQDs/GO-75 demonstrated the most favorable effect (Fig. S3). Thus, CNQDs/GO-75 was chosen as the

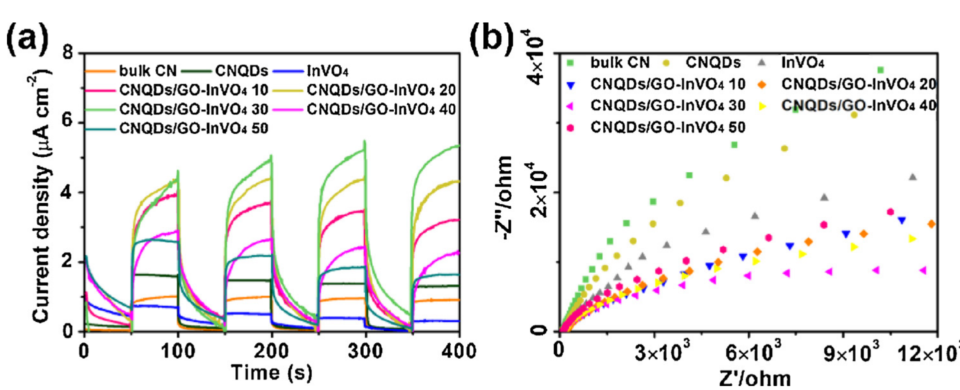


**Fig. 7.** (a) Photocurrent transient response and (b) electrochemical impedance spectra (EIS) of samples.

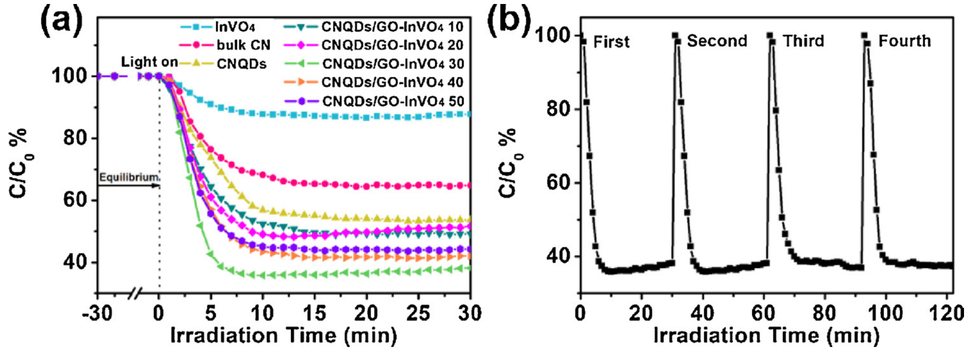


**Fig. 8.** (a) Photocatalytic activities of $InVO_4$, bulk CN, CNQDs and CNQDs/GO-$InVO_4$ aerogels for NO removal in air under visible-light irradiation, (b) multiple cycles of photocatalytic reactions over CNQDs/GO-$InVO_4$ 30 aerogel.

substrate to determine the effect of $InVO_4$. In these experiments, the photodegradation of NO on the pure $InVO_4$ cubes was only 14%, while the NO removal ratios of bulk CN and CNQDs were 34% and 45%, respectively, which was attributed to the good electrical conductivity of CNQDs. As expected, the photocatalytic activities of CNQDs/GO aerogels were enhanced substantially by the introduction of $InVO_4$, especially when the mass ratio of $InVO_4$ was 30%. The results demonstrated that the fabrication of a heterojunction strongly improved the photocatalytic activity. The aerogels with $InVO_4$ contents of 10%, 20%, 30%, 40% and 50% achieved NO removal efficiencies of 51%, 52%, 65%, 59% and 56%, respectively, as shown in Fig. 8a. Thus, the enhancement of the photocatalytic effect depends on choosing the optimal proportions of the two semiconductors. The stability of the photocatalyst is another important factor for practical application. Therefore, a multiple-cycle experiment was carried out over CNQDs/GO-$InVO_4$ 30 aerogel. Encouragingly, the NO removal ratio of CNQDs/GO-$InVO_4$ 30 aerogel remained high, with virtually no decrease after four repeated runs, as displayed in Fig. 8b. The estimated apparent quantum efficiency of NO removal was calculated as 1.8% according to the reported references [53–54], which demonstrated the good performance in the removal of NO by CNQDs/GO-$InVO_4$ aerogels.

### 3.6. Photocatalytic mechanism

To identify the active radicals that participate in the photodegradation of NO, ESR spin-trapping spectra were recorded with the DMPO technique to detect the superoxide radicals (DMPO-$\cdot O_2^-$) in methanol and hydroxyl radicals (DMPO-$\cdot$OH) in aqueous solution. As shown in Fig. 9, no characteristic peaks of $\cdot O_2^-$ or $\cdot$OH were detected in the absence of light. However, under visible-light irradiation, signals of DMPO-$\cdot O_2^-$ were observed, and four characteristic peaks of $\cdot$OH with the intensity ratio of 1:2:2:1 were also detected, indicating that both $\cdot O_2^-$ and $\cdot$OH are generated during this reaction.

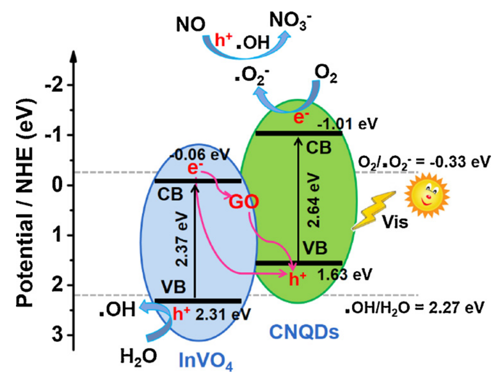


**Fig. 10.** Photocatalytic mechanism of NO removal by CNQDs/GO-$InVO_4$ aerogels under visible-light irradiation.

Based on the above ESR spin-trapping experiments and the calculated VB XPS results, a photocatalytic mechanism was proposed, as illustrated in Fig. 10. The VB positions of CNQDs and $InVO_4$ were 1.63 and 2.31 eV *vs* NHE, respectively, which were determined by the VB-XPS, as shown in Fig. 6c. Then the CB edges of CNQDs and $InVO_4$ were calculated to be −1.01 and −0.06 eV *vs* NHE, respectively. Both CNQDs and $InVO_4$ will generate photoinduced electrons and holes under visible-light irradiation. In the traditional charge-carrier transfer theory, the photogenerated $e^-$ in the CB of CNQDs would migrate to the CB of $InVO_4$, and the photogenerated $h^+$ in the VB of $InVO_4$ would migrate to the VB of CNQDs. However, the $e^-$ on the CB of $InVO_4$ cannot react with $O_2$ to form $\cdot O_2^-$ radicals because the position of CB is more positive than the potential of $O_2/\cdot O_2^-$ ($O_2/\cdot O_2^-$ = −0.33 eV *vs* NHE). Likewise, the $h^+$ on the VB of CNQDs is lower than the redox potential of $\cdot$OH ($\cdot OH/H_2O$ = 2.27 eV, *vs* NHE). Consequently, a Z-scheme transfer mechanism is proposed for this photodegradation

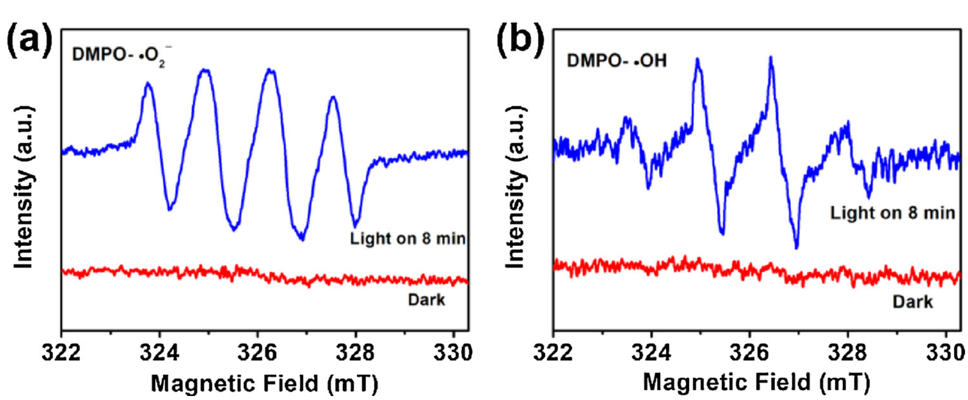


**Fig. 9.** DMPO spin-trapping ESR spectra of CNQDs/GO-$InVO_4$ 30 aerogel under visible-light irradiation for 8 min in (a) methanol solution for $\cdot O_2^-$ and (b) aqueous solution for $\cdot$OH.

process. In this mechanism, the $e^-$ in the CB of $InVO_4$ quickly migrates to the VB of CNQDs *via* the conductive material GO and reacted with the photoexcited holes of CNQDs. The accumulated $e^-$ in the CB of CNQDs will reduced $O_2$ to $\cdot O_2^-$, and the $h^+$ on the VB of $InVO_4$ reacted with $H_2O$ to form $\cdot OH$, which are crucial for NO removal. Finally, the produced $\cdot O_2^-$, $\cdot OH$ and $h^+$ together oxidize NO to $NO_3^-$. And the photocatalytic mechanism of NO removal by CNQDs/GO-$InVO_4$ aerogels were summarized in Eqs. (1)–(7), as the following:

$$\text{CNQDs/GO-InVO}_4 + h\nu \rightarrow \text{CNQDs}\ (e^-) + \text{InVO}_4\ (h^+) \tag{1}$$

$$3h^+ + NO + 2H_2O \rightarrow NO_3^- + 4H^+ \tag{2}$$

$$e^- + O_2 \rightarrow \cdot O_2^- \tag{3}$$

$$\cdot O_2^- + 2H^+ + 2e^- \rightarrow \cdot OH + OH^- \tag{4}$$

$$2\cdot OH + NO \rightarrow NO_2 + H_2O \tag{5}$$

$$NO_2 + \cdot OH \rightarrow NO_3^- + H^+ \tag{6}$$

$$NO + \cdot O_2^- \rightarrow NO_3^- \tag{7}$$

## 4. Conclusion

In summary, exfoliation technology and a template-free hydrothermal method were utilized in the fabrication of the novel 3D CNQDs/GO-$InVO_4$ aerogel. A series of aerogels were synthesized and all showed excellent photocatalytic activity towards the photocatalytic degradation of NO at the ppb-level, especially the CNQDs/GO-$InVO_4$ 30 aerogel, which exhibited the best efficiency of 65%. The superior efficiency is attributed to the interconnected layered structure of the aerogel, the construction of a heterojunction, the large degree of absorption of visible light, the outstanding conductivity, and the low recombination efficiency of $e^-$-$h^+$ pairs. The prepared macro-materials are stable and recyclable, demonstrating their potential application value in the extensive air purification field.

## Acknowledgements

We gratefully acknowledge the financial support provided by the National Key R&D Program of China (2017YFC0210901, 2017YFC0210906), National Natural Science Foundation of China (51573122, 21722607, 21776190), Natural Science Foundation of the Jiangsu Higher Education Institutions of China (17KJA430014, 17KJA150009), Science and Technology Program for Social Development of Jiangsu (BE2015637), and the project supported by the Priority Academic Program Development of Jiangsu Higher Education Institutions (PAPD).

## Appendix A. Supplementary data

Supplementary material related to this article can be found, in the online version, at doi:https://doi.org/10.1016/j.apcatb.2018.04.080.

## References

[1] J.H. Seinfeld, S.N. Pandis, J. Am. Chem. Soc. 121 (1999) 1423–1424.
[2] T. Xiong, T. Leveque, M. Shahid, Y. Foucault, S. Mombo, C.J. Dumat, Environ. Qual. 43 (2014) 1593–1600.
[3] B.N. Duncan, A.I. Prados, L.N. Lamsal, Y. Liu, D.G. Streets, P. Gupta, E. Hilsenrath, R.A. Kahn, J. Eric Nielsen, A.J. Henze, C.A. Hostetler, N.A. Krotkov, P. Lee, M. Lin, S. Pawson, G. Pfister, K.E. Pickering, R. Bradley Pierce, Y. Yoshida, L.D. Ziemba, Atmos. Environ. 94 (2014) 647–662.
[4] H. Du, L. Kong, T. Cheng, J. Chen, J. Du, L. Li, X. Xia, C. Leng, G. Huang, Atmos. Environ. 45 (2011) 5131–5137.
[5] K.-F. Ho, S.S.H. Ho, R.-J. Huang, H.-C. Chuang, J.-J. Cao, Y. Han, K.-H. Lui, Z. Ning, K.-J. Chuang, T.-J. Cheng, S.-C. Lee, D. Hu, B. Wang, R. Zhang, Atmos. Environ. 126 (2016) 162–170.
[6] L. Li, Q. Tan, Y. Zhang, M. Feng, Y. Qu, J. An, X. Liu, Environ. Pollut. 230 (2017) 718–729.
[7] J.J. Schauer, M.P. Fraser, G.R. Cass, B.R.T. Simoneit, Environ. Sci. Technol. 36 (2002) 3806–3814.
[8] L. Aidaoui, A.G. Triantafyllou, A. Azzi, K.G. Garas, V.N. Matthaios, Air Qual. Atmos. Health 8 (2015) 213–227.
[9] J. Schwartz, F. Laden, A. Zanobetti, Environ. Health Perspect. 110 (2002) 1025–1029.
[10] J. Tao, L. Zhang, J. Cao, L. Zhong, D. Chen, Y. Yang, D. Chen, L. Chen, Z. Zhang, Y. Wu, Y. Xia, S. Ye, R. Zhang, Sci. Total Environ. 574 (2017) 1559–1570.
[11] R.-J. Huang, Y. Zhang, C. Bozzetti, K.-F. Ho, J.-J. Cao, Y. Han, K.R. Daellenbach, J.G. Slowik, S.M. Platt, F. Canonano, P. Zotter, R. Wolf, S.M. Pieber, E.A. Bruns, M. Crippa, G. Ciarelli, A. Piazzalunga, M. Schwikowski, G. Abbaszade, J. Schnelle-Kreis, R. Zimmermann, Z. An, S. Szidat, U. Baltensperger, I.E. Haddad, A.S.H. Prevot, Nature 514 (2014) 218–222.
[12] G. Dong, W. Ho, Y. Li, L. Zhang, Appl. Catal. B: Environ. 174–175 (2015) 477–485.
[13] F. He, G. Chen, J. Miao, Z. Wang, D. Su, S. Liu, W. Cai, L. Zhang, S. Hao, B. Liu, ACS Energy Lett. 1 (2016) 969–975.
[14] W. Zou, Y. Shao, Y. Pu, Y. Luo, J. Sun, K. Ma, C. Tang, F. Gao, L. Dong, Appl. Catal. B: Environ. 218 (2017) 51–59.
[15] T. Xiong, W. Cen, Y. Zhang, F. Dong, ACS Catal. 6 (2016) 2462–2472.
[16] E.S.D. Silva, N.M.M. Moura, M.G.P.M.S. Neves, A. Coutinho, M. Prieto, C.G. Silva, J.L. Faria, Appl. Catal. B: Environ. 221 (2018) 56–69.
[17] X. Shi, M. Fujitsuka, Z. Lou, P. Zhang, T. Majima, J. Mater. Chem. A. 5 (2017) 9671–9681.
[18] C. Li, Y.Du.D. Wang, S. Yin, W. Tu, Z. Chen, M. Kraft, G. Chen, R. Xu, Adv. Funct. Mater. 27 (2017) 1604328.
[19] W.-J. Ong, L.-L. Tan, Y.H. Ng, S.-T. Yong, S.-P. Chai, Chem. Rev. 116 (2016) 7159–7329.
[20] Y.-N. Liu, C.-C. Shen, N. Jiang, Z.-W. Zhao, X. Zhou, S.-J. Zhao, A.-W. Xu, ACS Catal. 7 (2017) 8228–8234.
[21] Y. Kofuji, Y. Isobe, Y. Shiraishi, H. Sakamoto, S. Tanaka, S. Ichikawa, T. Hirai, J. Am. Chem. Soc. 138 (2016) 10019–10025.
[22] G. Dong, L. Yang, F. Wang, L. Zang, C. Wang, ACS Catal. 6 (2016) 6511–6519.
[23] Q. Xu, B. Cheng, J. Yu, G. Liu, Carbohydrate Res. 118 (2017) 241–249.
[24] G. Jiang, X. Li, M. Lan, T. Shen, X. Lv, F. Dong, S. Zhang, Appl. Catal. B: Environ. 205 (2017) 532–540.
[25] L. Ge, C. Han, X. Xiao, L. Guo, Appl. Catal. B: Environ. 142–143 (2013) 414–422.
[26] Z. Wang, Y. Huang, L. Chen, M. Chen, J. Cao, W. Ho, S.C. Lee, J. Mater. Chem. A. 6 (2018) 972–981.
[27] M.-Y. Ye, Z.-H. Zhao, Z.-F. Hu, L.-Q. Liu, H.-M. Ji, Z.-R. Shen, T.-Y. Ma, Angew. Chem. Int. Ed. 56 (2017) 8407–8411.
[28] J. Ma, C. Wang, H. He, Appl. Catal. B: Environ. 184 (2016) 28–34.
[29] K. He, J. Xie, M. Li, X. Li, Appl. Surf. Sci. 430 (2018) 208–217.
[30] X. Li, R. Shen, S. Ma, X. Chen, J. Xie, Appl. Surf. Sci. 430 (2018) 53–107.
[31] K. Qi, B. Cheng, J. Yu, W. Ho, J. Alloys Compd. 727 (2017) 792–820.
[32] R. Shen, J. Xie, H. Zhang, A. Zhang, X. Chen, X. Li, ACS Sustain. Chem. Eng. 6 (2018) 816–826.
[33] K. Qi, B. Cheng, J. Yu, W. Ho, Chin. J. Catal. 38 (2017) 1936–1955.
[34] X. Zhang, H. Wang, H. Wang, Q. Zhang, J. Xie, Y. Tian, J. Wang, Adv. Mater. 26 (2014) 4438–4443.
[35] X. Chen, Q. Liu, Q. Wu, P. Du, J. Zhu, S. Dai, S. Yang, Adv. Funct. Mater. 26 (2016) 1719–1728.
[36] A. Bandyopadhyay, D. Ghosh, N.M. Kaley, S.K. Pati, J. Phys. Chem. C. 121 (2017) 1982–1989.
[37] G. Li, Z. Lian, W. Wang, D. Zhang, H. Li, Nano Energy 19 (2016) 446–454.
[38] L. Sun, T. Du, C. Hu, J. Chen, J. Lu, Z. Lu, H. Han, ACS Sustain. Chem. Eng. 5 (2017) 8693–8701.
[39] L. Qu, N. Wang, H. Xu, W. Wang, Y. Liu, L. Kuo, T.P. Yadav, J. Wu, J. Joyner, Y. Song, H. Li, J. Lou, R. Vajtai, P.M. Ajayan, Adv. Funct. Mater. 27 (2017) 1701714.
[40] Z. Wang, Y. Huang, W. Ho, J. Cao, Z. Shen, S.C. Lee, Appl. Catal. B: Environ. 199 (2016) 123–133.
[41] Y. Tian, B. Chang, J. Lu, J. Fu, F. Xi, X. Dong, ACS Appl. Mater. Interfaces 5 (2013) 7079–7085.
[42] M.Q. Wen, T. Xiong, Z.G. Zang, W. Wei, X.T. Tang, F. Dong, Opt. Express 24 (2016) 10205–10212.
[43] X. Zhang, J. Zhang, J. Yu, Y. Zhang, Z. Cui, Y. Sun, B. Hou, Appl. Catal. B: Environ. 220 (2018) 57–66.
[44] Z. You, Y. Su, Y. Yu, H. Wang, T. Qin, F. Zhang, Q. Shen, H. Yang, Appl. Catal. B: Environ. 213 (2017) 127–135.
[45] Q. Guo, Y. Zhang, H.-S. Zhang, Y. Liu, Y.-J. Zhao, J. Qiu, G. Dong, Adv. Funct. Mater. 27 (2017) 1703711.
[46] L. Tang, C.-T. Jia, Y.-C. Xue, L. Li, A.-Q. Wang, G. Xu, N. Liu, M.-H. Wu, Appl. Catal. B: Environ. 219 (2017) 241–248.
[47] W. Wan, S. Yu, F. Dong, Q. Zhang, Y. Zhou, J. Mater. Chem. A. 4 (2016) 7823–7829.
[48] M.M. Islam, C.M. Subrmaniyam, T. Akhter, S.N. Faisal, A.I. Minett, H.K. Liu, K. Konstantinov, S.X. Dou, J. Mater. Chem. A. 5 (2017) 5290–5302.
[49] Y. Hou, Z. Wen, S. Cui, X. Feng, J. Chen, Nano Lett. 16 (2016) 2268–2277.
[50] Y. Xu, H. Bai, G. Lu, C. Li, G. Shi, J. Am. Chem. Soc. 130 (2008) 5856–5857.
[51] Z. Tong, D. Yang, J. Shi, Y. Nan, Y. Sun, Z. Jiang, ACS Appl. Mater. Interfaces 7 (2015) 25693–25701.
[52] Y. Meng, Y. Hong, C. Huang, W. Shi, CrystEngComm. 19 (2017) 982–993.
[53] H. Yan, J. Yang, G. Ma, G. Wu, X. Zong, Z. Lei, J. Shi, C. Li, J. Catal. 266 (2009) 165–168.
[54] Y. Gao, Y. Wang, H. Zhang, Appl. Catal. B: Environ. 178 (2015) 29–36.